Geoscientific
Model Development
Discussions

Open Access

EGU

1 **ShellTrace v1.0 - A new approach for modelling growth and trace element uptake in marine**

2 **bivalve shells: Model verification on pacific oyster shells (*Crassostrea gigas*)**

3 *de Winter, Niels J.*

4 Analytical, Environmental and Geochemistry (AMGC) Department, Vrije Universiteit Brussel, Pleinlaan 2, 1050
5 Brussels, Belgium

6

Geoscientific
Model Development
Discussions

7   **Abstract**

8   Bivalve shells record changes in their environment in the chemical composition of their shells and are

9   frequently used as paleoclimate archives. However, many studies have shown that physiological changes

10   related to growth of the bivalve may overprint these chemical tracers. In the present study, a new approach is

11   presented that models growth and development of bivalve shells without a priori knowledge of the physiology

12   of the species. The model uses digitized growth increments in a cross section of the shell together with basic

13   assumptions of the shape of the shell in order to model changes in shell length, thickness, volume, mass and

14   growth rate at a daily resolution through the lifetime of the bivalve. This approach reconstructs the growth

15   history of bivalves based on their shell without the need for a culture experiment, paving the way for growth

16   rate estimations based on fossil bivalve shells. Combination of the growth model with 2D X-Ray Fluorescence

17   trace element mapping allows the incorporation of trace elements into the shell to be modelled in 3D through

18   the bivalve's lifetime. This approach yields records of integrated total-shell trace element concentrations and

19   accumulation rates, which shed light on the rates and mechanisms by which these trace elements are

20   incorporated into the shells of bivalves. Application of growth and trace element modelling on a set of modern

21   pacific oyster shells of well-known origin and comparison of model results with conventional trace element

22   transects highlights the importance of considering heterogeneity in mineralogy, mineralization rates and

23   chemical composition within the shells of bivalves. These insights lead to a better understanding of the

24   complexity of trace element concentrations in bivalve shells, which can then be applied as proxies for the

25   reconstruction of sub-annual changes in palaeoenvironmental conditions over geological timescales.

26

Geoscientific
Model Development
Discussions

Open Access

EGU

1. Introduction

The study of climate and environmental change over geological timescales has yielded various important

insights into the dynamics of climate systems on Earth (e.g. Huber et al., 1995; Hesselbo et al., 2000; Zachos et

al., 2001; Wang et al., 2001; Sluijs et al., 2006). The knowledge about the sensitivity of Earth's climate and

environment that results from these studies is indispensable for the prediction of future changes in Earth's

climate. The study of environmental changes relies both on proxy-based palaeoenvironmental reconstructions

(e.g. McDermott, 2004; Leng and Marshall, 2004; Zachos et al., 2006; Affek et al., 2008) and climate and

environmental modelling based on, and calibrated with, these reconstructions (e.g. Barron et al., 1984;

Kutzbach et al., 1989; Claussen et al., 2002; Andrews et al., 2012). Important archives for proxy-based

reconstructions of palaeoenvironment on a high temporal resolution are fast-growing carbonate records such

as speleothems and the fossil skeletal remains of calcifying organisms such as corals, brachiopods and molluscs

(Goreau, 1977; de Winter and Claeys, 2017; Ullmann et al., 2017; Vansteenberge et al., CHEMGEO; de Winter

et al., PPP). Mollusc shells have gained much attention in the last decades, because the calcite in these shells

has high fossilization potential, their populations are abundant and several studies have shown that chemical

proxies in these shells record changes in their environment (e.g. Klein et al., 1997; Schöne et al., 2003; Lazareth

et al., 2003; Gillikin et al., 2008). Stable isotope ratios of carbon and oxygen in the calcite shells of bivalve

molluscs are almost exclusively precipitated in equilibrium with the surrounding seawater and can thus be

used to trace changes in temperature, productivity and salinity on a seasonal scale (Klein et al., 1996; Kirby et

al., 1998; Goodwin et al., 2001; Ullmann et al., 2010). However, to disentangle the effects of these parameters

and to properly understand changes in the local environment, it is important to apply multi-proxy studies of

shell calcite (e.g. Takesue and van Geen, 2004; Ullmann et al., 2013; de Winter et al., PPP). It is for this reason

that bivalve sclerochronology studies have focused on understanding the relationships of trace element

concentrations in bivalve calcite with their environment (Lorrain et al., 2005; Wanamaker et al., 2008; Freitas

et al., 2009; Schöne et al., 2011). Since then, a range of trace element ratios (e.g. Mg/Ca, Sr/Ca, Ba/Ca, Mn/Ca

and Li/Mg) have been used as proxies for environmental parameters (Klein et al., 1996a; Lazareth et al., 2003;

Carré et al., 2006; Gillikin et al., 2008; Füllenbach et al., 2015; Vihtakari et al., 2017).

A few studies have focused on the development and chemical composition of modern oyster shells and its

relation to the environment (e.g. Palmer and Carriker, 1979; Carriker et al., 1980; Lee et al., 2008; Surge and

Lohmann, 2008; Ullmann et al., 2010; 2013). These studies have shown that oyster shells are composed mostly

of calcite occurring as foliated calcite layers, prismatic calcite and chalky calcite while the myostracum and

hinge ligament are made of aragonite (Stenzel, 1963; Palmer and Carriker, 1979). There is some discussion

about the role of these calcite mineral phases, whether their precipitation is controlled by environmental

conditions and whether changes in the precipitated mineral phase are paced to regular (solar or lunar) cycles

(Carriker et al., 1980; Kirby et al., 1998; Surge et al., 2001; Ullmann et al., 2010). It has even been proposed

that the mineralization of the chalky calcite phase in oyster shells is mediated by microbial activity (Vermeij,

2014). Beside mineralogy and chemistry of the shell, shell growth rate and dimensions vary widely between

63   individuals in response to several environmental factors such as growth space, substrate, food availability and

64   amount of predation (Galtsoff, 1964; Palmer and Carriker, 1979; Surge and Lohmann, 2008).

65   All these physiological changes, such as variations in growth and metabolic rate, shell mineralogy and

66   spawning events, which affect the incorporation of trace elements into the shell of bivalves, complicate the

67   use of trace element records to complement environmental reconstruction by stable isotope

68   sclerochronology, (Klein et al., 1996b; Gillikin et al., 2005; Immenhauser et al., 2005; Freitas et al., 2006).

69   Furthermore, several studies have shown that rates by which trace elements are incorporated into bivalve

70   shells and the degree to which these rates are controlled by environmental factors can be vastly different

71   between different bivalve species (Reinfelder et al., 1997; Steuber, 1999; Richardson et al., 2004; Carré et al.,

72   2006). To constrain such variations in physiological parameters on the chemistry of bivalve shells, species-

73   specific culture experiments are carried out under controlled circumstances so relationships between

74   environmental parameters and shell chemistry can be precisely determined (e.g. Wang and Fisher, 1996;

75   Freitas et al., 2006; Gillikin et al., 2006). Such experiments can only be executed on extant bivalves, which

76   severely limits the potential to apply the acquired proxy transfer functions to reconstruct climate and

77   environment in pre-Cenozoic times (e.g. de Winter et al., PPP). In this study, a model is introduced that

78   approximates the development of a range of size parameters in the bivalve shell through ontogenetic age,

79   based solely on digitized coordinates of recognized annual shell increments in a longitudinal cross section

80   through the shell. Additionally, the modelled growth development and recruitment pattern in the shell cross

81   section is then superimposed on an XRF trace element map to model the incorporation of trace elements into

82   the shell with age. The application of this growth and trace element model is demonstrated on a set of shells

83   of the modern pacific oyster (*Crassostrea gigas*) with well-known origins and dimensions. Model results are

84   compared with conventional trace element analyses on line scans through the hinge of the shells as well as

85   with results from previous bivalve growth studies.

86   **2. Materials and Methods**

87   **2.1 Specimen acquisition and preparation**

88   A set of eight modern pacific oyster (*Crassostrea gigas*) shells were obtained from restaurant Jardin van Gogh

89   in Brussels, Belgium (http://www.jardinvangogh.be). The oysters originate from a cultivation area in coastal

90   Normandy (France, 49°4.0' N latitude and 1°35.47' W longitude) and were harvested on February 13th 2017.

91   The shells were rinsed with acetone (C_3H_5OH) and distilled water, cleaned superficially with a soft brush and in

92   an ultrasonic bath and oven dried overnight at 50°C. Dried shells were weighed on a digital scales ($\sigma = 0.01$ g),

93   their dimensions (shell length, maximum shell width, maximum shell thickness) were measured using digital

94   callipers ($\sigma = 0.01$ mm) and their volume was determined by water displacement measurement using a graded

95   cylinder. All shells were embedded in Araldite® 2020 epoxy resin (Huntsman, Basel, Switzerland), sectioned

96   longitudinally along their axis of maximum growth using a slow rotating, diamond coated saw ($\varnothing = 1$ mm) and

97   high-grade polished using silicon carbide polishing disks (up to P2400 grain size). Polished shell surfaces were

98   imaged by colour scanning (RGB) using an Epson® 1850 flatbed scanner (Seiko Epson Corp., Nagano, Japan) at

99   a pixel resolution of 6400 dpi (± 4 µm pixel size).

2.2 X-Ray Fluorescence measurements

101   Concentrations of calcium (Ca), silicon (Si), magnesium (Mg), strontium (Sr), zinc (Zn), sulphur (S), phosphorous

102   (P), manganese (Mn) and iron (Fe) were measured on the polished shell surfaces using a Bruker® M4 Tornado

103   micro-X-ray Fluorescence scanner (Bruker GmbH, Berlin, Germany) equipped with a Rh X-Ray source using

104   maximum energy settings (50 kV, 600 µA) with a spot size of 25 µm (Mo Kα) and two Silicon Drift detectors.

105   The XRF setup is described in detail in de Winter and Claeys (2017). The entire shell surface was mapped semi-

106   quantitatively by XRF scanning in mapping mode using 1 ms integration time per pixel (as described in de

107   Winter and Claeys, 2017). Spacing between pixels was chosen in such a way that the total amount of pixels per

108   map was relatively constant ($\pm 4.0 \times 10^6$) for all shells while choosing the minimum rectangular area that

109   contained the entire cross section area. This caused pixel spacing in maps to vary between 25 µm (interlocking

110   X-Ray spots) and 30 µm. Quantitative XRF line scans were carried out on the dense foliated calcite layers in the

111   hinges of all shells perpendicular to the growth layers (see Palmer and Carriker, 1979) using the point-by-point

112   scanning method outlined in de Winter et al. (in review, PPP) with an integration time of 60 seconds per point.

113   This integration time allowed enough count statistics for the instrument to reach the Time of Stable

114   Reproducibility (TSR) and provide reproducible trace element concentrations for the elements of interest (de

115   Winter et al., 2017). All XRF line scans were quantified using the Bruker Esprit® fundamental parameters (FP)

116   quantification relative to the BAS CRM 393 limestone standard. Errors of reproducibility of µXRF

117   measurements are generally higher than the instrumental error and depend on the integration time and the

118   excitation energy of the element (see de Winter and Claeys, 2017; de Winter et al., 2017). Typical

119   reproducibility errors of µXRF point measurements are reported in **Table 3**.

2.3 Data preparation

121   Concentrations (in µg/g) of trace elements were calculated for profiles measured using XRF and plotted using

122   Grapher™ 8 (Golden Software Inc., Golden, CO, USA) graphing software. Timing of shell deposition was

123   inferred from annual cyclicity in trace element profiles. Growth increments (lines of simultaneous deposition in

124   the shell) were digitized on high-resolution colour scans of polished shell cross sections of the shells using the

125   pen tool in Adobe Illustrator® CC 17.1.0 (Adobe Systems Inc., San Jose, USA). Outlines of the rectangular area

126   of the cross section mapped by XRF were digitized in the same way. Line coordinates were saved in a SVG-file,

127   which allowed X-and Y-coordinates of the lines to be extracted and ordered into a comma separated (CSV) file

128   to be imported into the modelling script (**Step 1** in **Fig. 1**). An example of a shell cross section with traced

129   growth increments is shown in **Figure 2**. SVG- and CSV files of growth increments digitized in all shells used in

130   this study are found in **supplementary data 1**.

131   XRF map data was processed using Bruker Esprit® software. Maps were subject to a PCA-assisted maximum

132   likelihood phase analysis using a selection of distinctive elements (Ca, Mg, Sr, P, S and Mn). Minimum phase

Geoscientific
Model Development
Discussions

133   area was fixed to 0.05% of the total map area. Phase analysis results were matched with interpreted growth

134   increments and high-resolution colour scans and associated phases were merged. Sum XRF spectra of all pixels

135   in each phase were quantified relative to the BAS CRM 393 standard using Esprit® software. Minimum area of

136   each phase was such that the total integration time contained in all the pixels allowed Time of Stable

137   Reproducibility to be reached for the quantification of the sum spectrum (de Winter et al., 2017). Phase maps

138   were exported as BMP files and oriented in the same way as colour scans with the shell hinge facing left and

139   the inside of the shell facing down (see **Fig. 2**).

140   **2.4 Modelling approach**

141   A modelling routine was written in the open source computational software package R (R Core Team, 2013)

142   using Microsoft® Visual Studio Code Version 1.10.2. Shell growth and trace element accumulation rates were

143   modelled in six steps, of which **Step 1** is a data preparation step (see above), **Step 2-4** form the growth model

144   and **Step 5-6** make up the trace element model (**Fig. 1**). The complete R-script used for the model is provided

145   in **supplementary data 2**. Variables used in the modelling process are indicated in **Figure 3**.

146

147   **2.4.1 Growth modelling**

148   **Step 2** of the model converts X- and Y-coordinates of all digitized increments to millimetres using the ratio

149   between the real length of the digitized image and the length in pixels. All increments are converted to one

150   cross section matrix (*Digitized cross section*) with a common X-axis with a default step size (*dx*) using linear

151   interpolation between line segments. The resulting cross section is plotted to provide a check on the model

152   progress. From this matrix, the area between each increment and its predecessor is calculated using the

153   formula:

154                     $$\textbf{F1}: \boldsymbol{O_i = \int_{x_0}^{x_{end}} Y_{i-1}(x) - Y_i(x)\, dx} \qquad (1)$$

155   in which O_i is the area between increment *i* and increment *i*-1, x_0 and x_{end} are the extreme values of the range

156   of X coordinates in *Digitized cross section* and Y_i and Y_{i-1} are the Y-coordinates of increment *i* and *i*-1

157   respectively. Y_{i-1} is always bigger than Y_i since bivalves build their shell by adding material on the inside of the

158   shell, which faces down in this model. The average shell thickness at each increment is determined using the

159   formula:

160                     $$\textbf{F2}: \boldsymbol{T_i = \frac{\sum_{x_0}^{x_{end}} Y_0(x) - Y_i(x)}{x_{end} - x_0}} \qquad (2)$$

161   in which T_i is the average thickness of the shell at increment *i*, $Y_i(x)$ and $Y_0(x)$ are the Y-coordinates of

162   increment *i* and the top of the shell (increment 0). Total shell length is calculated from the X- and Y-

163   coordinates of the start- and endpoints of the increment (where the increment meets the top or bottom of the

164   shell) and the Pythagorean Theorem following the formula:

165                     $$\textbf{F3}: \boldsymbol{L_i = \sqrt{(x_e - x_s)^2 + (Y_e - Y_s)^2}} \qquad (3)$$

Geoscientific
Model Development
Discussions

166   in which L_i is the length of the shell at increment i, x_s, x_e, Y_s and Y_e are the X- and Y-coordinates of the start- and

167   endpoints of the increment *i*. The results of these calculations, as well as values for x_s, x_e, Y_s and Y_e are stored

168   in a *Matrix of parameters by increment*.

169   **Step 3** of the growth model takes *Digitized cross section*, *Matrix of parameters by increment* and a

170   customizable number of increments (*N*) to be interpolated to create a new cross section matrix with *N-1*

171   interpolated sub-increments between each set of increments (*Sub-incremental cross section*). Interpolation of

172   sub-increments is done by linear interpolation of the Y-coordinate of sub-increments between that of the two

173   increments (see insert in **Figure 3A**) according to the following formula:

174   $$\textbf{F4.1}: \left[\left[Y_t(x) = Y_{i-1}(x) - \frac{n}{N} * \left(Y_{i-1}(x) - Y_i(x)\right)\right]_{n=0}^{n=N-1}\right]_{x=x_0}^{x=x_{end}} \qquad (4)$$

175   With

176   $$\textbf{F4.2}: t = i - 1 + \frac{n}{N} \qquad (5)$$

177   in which $Y_t(x)$ is the Y-coordinate of the nth sub-increment between increment i and increment i-1 and x_0 and

178   x_{end} are the extreme values of range of X-values in *Digitized cross section* (as in **F1**). All calculated values for

179   $Y_t(x)$ are stored with reference to their sub-increment number (*t*) and X-coordinate in the new *Sub-incremental*

180   *cross section* matrix. The resulting cross section is plotted to provide a check on the model progress. This new

181   matrix is then used to calculate area between sub-increments, shell thickness and total shell length during

182   deposition of each sub-increment by formula **F1**, **F2** and **F3** respectively. Additionally, using the measured

183   maximum length (*Shell length*) and width (*Shell width*) of the oyster, parameters *a* and *b* of the ellipse that

184   forms the base of the shell for volume calculations (**Figure 3B**) are calculated according to formulae:

185   $$\textbf{F5.1}: a_t = \frac{1}{2} * \frac{W_{max}}{L_{max}} * (x_e - x_s) \qquad (6)$$

186   $$\textbf{F5.2}: b_t = \frac{1}{2} * (x_e - x_s) \qquad (7)$$

187   in which a_t and b_t are the parameters *a* and *b* of the ellipse that forms the base of the shell at sub-increment *t*,

188   L_{max} and W_{max} are the maximum length and width of the oyster shell and x_s and x_e are the X-coordinates of the

189   start- and endpoints of the increment *t* (as in **F3**). All these parameters are stored in *Matrix of parameters by*

190   *sub-increment* (**Figure 1**).

191   **Step 4** takes *Incremental cross section* and the ellipse parameters in the *Matrix of parameters by sub-*

192   *increment* to calculate the Z-values of the ellipse that forms the base of the shell at each sub-increment (see

193   **Figure 3B**). The Z-value is defined as the distance between the edge of the ellipse and the X-axis through the

194   shell (**Figure 3B**), and is calculated by the following formula, which is an adaptation of the standard formula for

195   ellipsoids:

196   $$\textbf{F6.1}: \left(\frac{Z_t(x)}{a_t}\right)^2 + \left(\frac{x^*_t}{b_t}\right)^2 = 1 \rightarrow$$

Geoscientific
Model Development
Discussions

197 $$\textbf{F6.2}: \boldsymbol{Z_t(x) = \left(\frac{a_t}{b_t}\right) * \sqrt{{b_t}^2 - {x^*_t}^2}} \qquad (8)$$

198 in which Z_t is the Z-value (distance from X-axis) of the ellipse at X-coordinate x^*_t for sub-increment t, a_t and b_t

199 are the parameters of the ellipse at sub-increment t and x^*_t is the X-coordinate relative to the centre of the

200 ellipse, and is calculated by

201 $$\textbf{F6.3}\; \boldsymbol{x^*_t = x - x_s - b_t} \qquad (9)$$

202 All Z-values are saved in a matrix (*Z-values* in **Figure 1**) with reference to their increment numbers (*t*) and X-

203 coordinates. Then, using the Z-values and the parameters from *Matrix of parameters by sub-increment*, shell

204 volume is calculated for each sub-increment. This is done by calculating areas between the sub-increment and

205 the top of the shell (sub-increment 0) in a cross sections through the shell perpendicular to the X-axis (in YZ-

206 plane, see **Figure 3C**) and multiplying these with the step size in X-direction (*dx*). This is done for every X-value,

207 and adding up all volume increments yields an estimate the total volume between the shell sub-increment and

208 the base of the shell:

209 $$\textbf{F7.1}: \boldsymbol{V_t = \int_{x_0}^{x_{end}} \left(A_0(x) - A_t(x)\right) dx} \qquad (10)$$

210 in which V_t is the volume of the shell at increment t and $A_0(x)$ and $A_t(x)$ are the area under increment t and

211 the top of the shell (increment 0) respectively in the cross section in YZ-direction (**Figure 3C**). These areas are

212 modelled for every X-value by constructing a circle section through the corresponding point on the sub-

213 increment in the XY cross section (centre of the YZ-cross section **Figure 3A**, or point **P1**)

214 $$P1[x, y_1, z_1] = [x, Y_t(x), 0] \qquad (11)$$

215 and the two points where the YZ-cross section intersects the ellipse that forms the base of the shell (see **Figure**

216 **3A** and **Figure 3C**):

217 $$P2[x, y_2, z_2] = [x, Y_{ellipse}(x), -Z_t(x)] \qquad (12)$$

218 $$P3[x, y_3, z_3] = [x, Y_{ellipse}(x), Z_t(x)] \qquad (13)$$

219 The value $Y_{ellipse}(x)$ is the Y-value of the ellipse with respect to the line y=0 (**Figure 3C**), which can be calculated

220 by linear interpolation of the slope of the ellipse using the start and end points of the sub-increment (x_s, x_e, Y_s

221 and Y_e) and *x*:

222 $$\textbf{F7.2}: \boldsymbol{Y_{ellipse} = Y_s + \left(\frac{Y_e - Y_s}{x_e - x_s}\right) * (x - x_s)} \qquad (14)$$

223 The centre of this circle is the point

224 $$P_c[x, y_c, z_c] = [x, Y_c, 0] \qquad (15)$$

225 its radius *r* is equal to the difference between $Y_t(x)$ and Y_c, and the circle can be described by the formulae:

226 $$\textbf{F7.3}: \boldsymbol{\Delta y^2 + \Delta z^2 = r^2} \rightarrow$$

Geoscientific
Model Development
Discussions
Open Access
EGU

227   **F7.4**: $(y_1 - y_c)^2 + (z_1 - z_c)^2 = (y_3 - y_c)^2 + (z_3 - z_c)^2 \rightarrow$

228   **F7.5**: $\left(Y_t(x) - Y_c(x)\right)^2 + (0 - 0)^2 = \left(Y_{ellipse}(x) - Y_c(x)\right)^2 + (Z_t(x) - 0)^2 \rightarrow$

229   **F7.6**: $Y_c(x) = \frac{(Y_t(x)^2 - Y_{ellipse}(x)^2 - Z_t(x)^2)}{2*\left(Y_t(x) - Y_{ellipse}(x)\right)}$ (16)

230   **F7.7**: $r_t(x) = \sqrt{Z_t(x)^2 + \left(Y_{ellipse}(x) - Y_c(x)\right)^2}$ (17)

231   With all parameters known, the area in the YZ-cross section under the sub-increment (between the circle

232   segment and the line y=0) can be calculated as the area of the section of the circle above the ellipse plus the

233   area of the rectangle between the ellipse and y=0 (**Figure 3C**). The angle θ describing this circle section is equal

234   to:

235   **F7.8**: $\theta = 2 * \sin^{-1}\left(\frac{Z_t(x)}{r_t(x)}\right)$ (18)

236   However, if point **P1** lies below the ellipse ($Y_t(x) < Y_{ellipse}(x)$; in the case of irregular shells that curve upwards

237   during growth), the centre of the circle lies above the shell and the area under the sub-increment is described

238   by subtracting the section of the circle above the ellipse from the area of the rectangle (see **Figure 3C**):

239   **F7.9**: $A_t = \begin{cases} A_{segment} + A_{rectangle} = \frac{1}{2}\left(r_t(x)\right)^2 * (\theta - \sin\theta) + 2 * Z_t(x) * Y_{ellipse}(x), \ Y_t(x) \geq Y_{ellipse}(x) \\ A_{rectangle} - A_{segment} = 2 * Z_t(x) * Y_{ellipse}(x) - \frac{1}{2}\left(r_t(x)\right)^2 * (\theta - \sin\theta), \ Y_t(x) < Y_{ellipse}(x) \end{cases}$ (19)

240   Net areas are calculated as the differences between the areas under the sub-increment *t* and the area under the

241   top of the shell (sub-increment 0), and volumes for sub-increments are calculated by integrating these areas

242   over *x* (see formula **F7.1** above). Shell growth rates are then calculated by multiplying the change in volume per

243   sub-increment with *Shell Density* (ρ):

244   **F8.1**: $\Delta M_t = \rho * (V_{t-1} - V_t)$ (20)

245   and absolute mass accumulation is calculated by simple multiplication of the modelled incremental volume

246   increase of the shell with *Shell Density*:

247   **F8.2**: $M_t = \rho * V_t$ (21)

248

249   **2.4.2 Trace element modelling**

250   **Step 5** of the model takes the BMP-file of the *Phase map* of the shell and a matrix of the quantified

251   concentrations of all elements of interest in each of the phases as well as their colour values (*Phase data*,

252   **Figure 1**) as input to convert the BMP image to a matrix of phases (*Phase matrix*, **Figure 1**). This matrix is then

253   used to export a table with statistics of the relative abundance of phases in the entire phase map (*Phase*

254   *statistics*, **Figure 1**). *Phase data* tables used as input to model every shell described in this study are given in

255   **supplementary data 3**.

256   **Step 6** uses this *Phase matrix* together with *Incremental cross section* to calculate the amount of pixels of each

257   phase that is contained in every sub-increment (*Sub-increment phase matrix*, **Figure 1**). From this data, the

258   concentration of each element in each sub-increment are calculated by multiplying the relative proportion of

259   each phase in the sub-increment by the quantified concentrations of all elements in that phase:

260   $$\textbf{F9}: \boldsymbol{C_t^E} = \sum_{p=p_1}^{p=p_n} \frac{S_p}{S_{tot}} * \boldsymbol{C_p^E} \text{ with } \boldsymbol{p} \text{ in } [\boldsymbol{p_1, p_2, p_3, \dots, p_n}] \qquad (22)$$

261   where C_t^E is the concentration of element *E* in sub-increment *t*, *p* is the phase (in p_1, p_2, p_3… …p_n), S_p is the

262   amount of pixels assigned to phase *p* in sub-increment *t*, S_{tot} is the total amount of pixels in sub-increment *t*,

263   and C_p represents the concentration of element E in phase p. The distribution of trace element concentrations

264   in each sub-increment is stored in *Matrix of concentration through time*. This matrix is then multiplied with a

265   smoothed record of modelled mass accumulation and growth rates (see **Step 4**, smoothing occurs via a

266   running average over the mass accumulation and growth rate records and the *Degree of smoothing* is

267   customizable and determines the window size of this running average) to calculate the cumulative

268   accumulation and accumulation rates, respectively, of all (trace) elements through time in the shell:

269   $$\textbf{F10.1}: \boldsymbol{M_t^E} = \boldsymbol{C_t^E} * \boldsymbol{M_t} \qquad (23)$$

270   $$\textbf{F10.2}: \left[\frac{\partial M}{\partial t}\right]_t^E = \boldsymbol{C_t^E} * \boldsymbol{N} * \boldsymbol{\Delta M_t} \qquad (24)$$

271   Matrices of modelled elemental concentrations (*Matrix of concentrations through time*), cumulative trace

272   element accumulation (*Cumulative elemental mass accumulation*) and accumulation rates (Elemental mass

273   accumulation rate) modelled through the shell's age are exported for further analysis. An overview of all

274   model functions and variables is given in **Table 1**. Exported matrices containing modelling results for every

275   shell featuring in this study are presented in **supplementary data 4**

276   **3. Results and discussion**

277   **3.1 XRF and shell dimension measurements**

278   Shells of *C. gigas* are highly irregular with considerable differences in shape between individuals, as is evident

279   from measurements of the shell dimensions (**Table 2**) and the colour scans of the shells (**Figure 2** and

280   **supplementary data**). Shell length, width, volume and mass vary considerably between *C. gigas* specimens and

281   estimated age based on proxy records is not a good predictor of shell size. Furthermore, the length-to-width

282   ratio is highly variable between shells, making size development in *C. gigas* hard to predict. Densities of *C.*

283   *gigas* shells are relatively low (ρ = 2.10 g*cm^{-1}) compared to the densities of shell-forming minerals such as

284   calcite (ρ = 2.71 g*cm^{-1}), aragonite (ρ = 2.95 g*cm^{-1}) and nacre (ρ = 2.60 g*cm^{-1}). This difference is most likely

285   caused by the presence of porosity in the shell structure, which should be around 23% to account for the

286   difference in shell density.

287   **Figure 2** shows the result of colour scanning, XRF mapping with phase analysis and a tracing of the growth

288   increments in a longitudinal cross section through one of the *C. gigas* shells. The shell depicted in **Figure 2** is

289   used as an example for the remainder of the results and discussion, while outcomes for the remaining seven

290   shells are disclosed in in **supplementary data 5**. **Figure 2** shows that phase analysis on the XRF map of oyster

291   shells results in the separation of four chemically distinct phases in the cross section. Comparison with the

292   colour scan shows that these phases represent dark foliated calcite layers in the shell (green), light chalky

293   calcite layers in the shell (blue), detrital inclusions in the edge of the shell (yellow) and the surrounding resin

294   (red). Trace element concentrations of the foliated and chalky calcite phases in each shell are found in **Table 3**.

295   Mapping and phase analysis in all shells resulted in a distinction between foliated calcite and chalky calcite

296   layers in terms of chemical composition (see **Figure 2** and compare chemical compositions in **Table 3**). The

297   phase map in **Figure 2** also shows that the hinge of the shell consists of foliated calcite. Traces of growth

298   increments in the oyster shell show once more that growth patterns in *C. gigas* are highly irregular. While shell

299   growth always happens by addition of material on the inside of the shell valve (facing down in **Figure 2**), shell

300   thickness varies strongly throughout the shell and shell extension rates vary both with age and with location in

301   the shell. Furthermore, oyster shells extend away from the shell hinge (to the right in **Figure 2**) as well as

302   towards the inside of the shell, making the hinge thicker with age (downward and to the left in **Figure 2**). These

303   shell characteristics complicate the modelling of shell growth and render *C. gigas* an ideal species for rigorous

304   testing of the model presented in this study.

305   Results of line scanning through the hinge of the oyster are shown in **Figure 4**. Shells of *C. gigas* are

306   characterized by periodic variations in concentrations of strontium (Sr), magnesium (Mg), sulphur (S), iron (Fe),

307   manganese (Mn) and zinc (Zn). Records of silicon (Si) and calcium (Ca) concentrations indicate which parts of

308   the records represent pure shell calcite (high [Ca], low [Si]) and which consist of calcite diluted with detrital

309   material (lower [Ca], [Si] > 2000 µg/g, mostly on the outside of the shell, see **Fig. 4**). Shell increments used as

310   tracers for growth modelling are generally characterized by decreased Ca and Mg concentrations and

311   increased concentrations of Fe, Mn, Zn and Sr. Furthermore, records of Sr and Zn show regular cyclicity, while

312   Fe and Mn records are characterized by sharp increases relative to a stable baseline. The Mg record shows

313   small scale variations inversely related to those in the Zn record. Periodic variations in the trace element

314   records allow the establishment of an age model for the growth of this oyster shell, as is shown in **Figure 4**.

315   Note that line scanning through the hinge of the shell only allows for the sampling of the last three growth

316   years, as the irregular shape of the oyster shell and the occurrence of chalky calcite further up the hinge

317   prevents the measurement of a complete record through the foliated calcite. Also note that growth

318   increments used as a basis for growth modelling are not paced to the seasonal cycle. The organisation of

319   isochronous growth increments in the colour scan on top of **Figure 4** shows the occurrence of chalky calcite

320   layers embedded between foliated calcite layers in some parts of the shell while these are absent in other

321   parts. This further confirms that multiple types of shell mineral phases (e.g. foliated calcite and chalky calcite)

322   can be precipitated in the shell simultaneously. Since mineral phases are chemically distinct (**Table 3**), this

323   observation warrants the consideration of the growth of both shell phases in an analysis of trace element

324   uptake by oyster shells, showing that simply analysing foliated calcite in the hinge of the shell may not yield a

325   complete understanding of the incorporation of trace elements into the shell.

326 **3.2 Growth model**

327 The output of the growth model applied on cross sections of *C. gigas* shells consists of records of shell length,

328 average thickness, volume, mass and growth rates through shell age (**Figure 5**). Tables containing the complete

329 records of all these parameters for all shells are given in **supplementary material 4**, and modelled shell

330 dimensions at the end of the modelling run are given in **Table 2**. **Figure 5** shows the records for the above

331 mentioned shell parameters plotted against age following the age model based on line scans through the shell

332 hinge. The results show that, though there is ample variation in size development between individuals, the

333 development of shell size parameters follow a similar pattern in all the examined shells. Development of shell

334 length in all modelled shells follows the asymptotic Von Bertalanffy growth model ($L = L_\infty * e^{-kt}$; Von

335 Bertalanffy, 1957). Parameters of Von Bertalanffy models (k and L_∞) fitted to shell length records of each shell

336 are given in **Table 2**. Results show that, while Bertalanffy curves fit the shell length development very well (R^2 >

337 0.90 for most shells except for #3 and #4), Bertalanffy's K values (k) as well as maximum shell lengths (L_∞) vary

338 strongly. This result is unsurprising for oyster shells, which are known to show large variations in growth rate

339 and morphology in response to local environmental constraints on their growth (Galtsoff, 1964; Palmer and

340 Carriker, 1979). Curve fitting through a composite of all *C. gigas* shells yields a maximum shell length of 102.34

341 mm and the growth curve constant (Bertalanffy's K) of 0.99. The values for maximum shell length are

342 significantly lower than the value found for sister-taxa *C. virginica* (150 mm; Rothschild et al., 1994), but this

343 may be a result of the use of relatively young individuals in this study. The fact that the obtained results seem

344 to fit the Von Bertalanffy model well (R^2 = 0.60 for all shells combined, see **Table 3** and **Figure 5**) shows that

345 the shell growth results produced by the model are reasonable, because it is known that the Von Bertalanffy

346 growth model describes shell length in most bivalves. The values for Bertalanffy's K fitting the model results

347 are quite high compared to most bivalve growth studies (e.g. Bachelet, 1980; MacDonald and Thompson,

348 1985; Hart and Chute, 2009), but values greater than 1 are not unheard of in bivalve species that show steep

349 growth curves early in life (e.g. Urban, 2000; Richardson et al., 2004). Modelled shell lengths closely resemble

350 those measured on the shell, with an average offset of 0.16 mm (0.16% relative to average shell length, see

351 **Table 2**) and are in good agreement with shell length measurements of living specimens of *C. gigas* (Diederich,

352 2006).

353 The development of other growth parameters shows similar variation within the same pattern of development

354 between individuals of *C. gigas*, attesting to the reproducibility of the growth model. For example, the average

355 shell thickness of oyster shells is best described by a linear increase in thickness with age (**Figure 5**). Individual

356 results show that the initial increase in thickness (slope of the average shell thickness curve) is quite variable,

357 but that later in life the different individuals of *C. gigas* converge towards a similar average shell thickness. This

358 results in rather variable rates of shell thickness increase between individuals (0.54–1.61 mm/yr, see **Table 2**).

359 The convergence of the shell thickness curves at later age suggests that this range is biased by the use in this

360 study of relatively young individuals. These differences in the development of shell thickness in oyster shells

361 are likely to be a result of spatial constraints on shell growth (Bartol et al., 1999). The agreement between the

362 final thicknesses of individuals is quite remarkable given their irregular shell shape and vastly different

363   proportions of shell length and width (**Table 2**). Maximum thickness (thickness of the thickest part of the shell)

364   is not modelled and therefore cannot be compared with measured values in **Table 2**, but modelled average

365   thicknesses are in agreement with observations in the cross section, and are proportional to measured

366   maximum thickness of the shells.

367   Modelled shell mass and volume development are best approximated by a polynomial increase with shell age

368   that is in agreement with the linear increase observed in modelled growth rates of *C. gigas*, which is naturally

369   the derivative of shell mass development (**Figure 5**). Modelled shell volume and mass at the end of the shell's

370   lifetime generally underestimate measured volume and mass by 4.2 cm^3 and 9.0 g respectively (±21%, see

371   **Table 2**). The most likely reason for this offset is that the assumption of a semi-circular shape of the YZ-plane

372   cross-section through the shell (perpendicular to the growth axis, see **Figure 3C**) underestimates the area of

373   this cross section. In reality, the decrease in shell thickness towards the outer margins of the shell is probably

374   less pronounced. Trends in volume and growth rates are less reproducible between individuals than those in

375   shell length and shell thickness, as is evident from the diverging polynomial fits that fit the model data. This

376   behaviour illustrates the erratic growth of *C. gigas* shells, which is also evident from the shape of their shell

377   (**Figure 2** and **supplementary data 5**). As is shown by the modelled growth rate curves (**Figure 5**), the growth

378   of these oyster shells is characterized by short-lived increases in growth rate followed by periods of slower,

379   more constant shell growth. The implications of these periodic growth spurts punctuating more constant

380   growth rates are also visible in the shell volume curves that often show stepwise increases in shell volume. To

381   a lesser extent, the same periodic growth is seen in the records of shell length and thickness. On a closer

382   examination, periods of faster growth rates can be associated with either contemporary increases in shell

383   length or in shell thickness, but rarely both at the same time. This strongly suggests a control of available

384   growth space on the shape and size development of *C. gigas* shells in competition with other individuals in an

385   oyster reef (e.g. Palmer and Carriker, 1979; Bartol et al., 1999). On the other hand, food availability is known to

386   significantly affect growth rates in bivalve shells (Kerswill, 1949; Coté et al., 1994; Surge and Lohmann, 2008),

387   showing that peaks in growth rate found by the model results in this study may be attributed to short-lived

388   increases in food availability commonly associated with algal blooms in spring and autumn in the region of

389   study (Edwards et al., 2001; Wiltshire et al., 2008). This reliance of shell growth on environmental factors

390   illustrates the potential of these model results to aid in the reconstruction of environmental conditions.

391   **3.3 Trace element model**

392   Records of trace element accumulation rates and total shell trace element concentrations that result from

393   trace element modelling are plotted for one of the *C. gigas* shells in **Figure 6** together with concentrations in

394   the hinge of the shell measured using XRF line scanning. Records of accumulation rates of different elements

395   show similar trends during shell growth and correlate with changes in shell growth rates. For some elements

396   (e.g. Zn and S) the total shell concentrations over time resemble concentrations measured in the hinge of the

397   shell, while for other elements (e.g. Mg and Sr) the total shell concentrations show a very different pattern

398   from the measured concentrations in the foliated calcite in the shell hinge. The reason for this difference is

399   that some elements (e.g. Zn and S) have very similar concentrations in the foliated calcite and the chalky

400   calcite layers, whereas these concentration can be very different for other elements (e.g. Mg and Sr; see **Table**

401   **3**). Since the type of mineral phase deposited during shell growth is not controlled by growth seasonality or

402   age (Surge et al., 2001; Titschack et al., 2008), differences in the degree of incorporation of mineral phases

403   over time will result in different total shell concentrations. These differences in total shell concentrations and

404   concentrations in the shell hinge illustrate the value of the proposed trace element modelling approach, as

405   concentrations taken up in the shell are better reflected by total shell concentrations than by concentrations in

406   one of the mineral phases in the shell. Furthermore, in combining the results of trace element modelling with

407   measurements on the shell hinge of bivalves, it is possible to constrain the relative amount of each mineral

408   phase that is incorporated into the shell at any given time. This allows the reconstruction of changes in shell

409   mineralogy and help isolate of the factors that control these changes, which is an important question in the

410   study of oyster growth (e.g. Currey and Taylor, 2000; Surge et al., 2001; Titschack et al., 2008;Beniash et al.,

411   2010).

412   **4. Conclusions and outlook**

413   This study proposes a new method of modelling the growth, development and trace element incorporation in

414   bivalve shell based on the location of growth increments in a cross section of the shell. The advent of a

415   working model that can independently constrain growth and trace element uptake rates would greatly benefit

416   the field of bivalve sclerochronology by providing independent control on shell growth rates, which influence

417   the expression of geochemical proxies in the shell. This development is especially interesting for studies

418   dealing with extinct bivalve species for which there are no modern analogues. The basic assumptions of the

419   model render it applicable on all bivalve species with the same general shape and growth direction. Growth

420   modelling following this numerical approach yields curves of shell development with age that resemble growth

421   curves established via *in vivo* measurements and allows the discussion of differences in growth and

422   development within and between bivalve species. The present modelling approach allows the comparison of

423   growth and development of bivalve shells on a sub-annual scale without a priori knowledge about growth

424   rates in the species, opening up the comparison of proxy records in fossil bivalves with records of growth rate

425   derived by applying this model. This allows the discussion of the applicability of trace element concentrations

426   as direct tracers of environmental change as opposed to being controlled by physiological processes related to

427   shell growth.

428   The combination of growth modelling with 2D trace element XRF mapping allows the projection of trace

429   element distribution to a 3D model of shell volume to numerically model the total shell concentration and

430   accumulation of trace elements into bivalve shells. Comparison between modelled total shell trace element

431   content and concentrations measured along the growth axis in the shell hinge following a conventional

432   measurement protocol reveals different patterns in trace element concentrations. This shows that

433   conventional trace element profiles through the shell hinge, recording only a small part of the shell, are not

434   always representative for total shell concentrations and that modelling these concentrations may shed more

435   light on the incorporation of trace elements into bivalve calcite. Further research should therefore consist of

436   applying this modelling approach in other bivalve studies to compare modelled and measured trace element

Geoscientific
Model Development
Discussions

437 concentrations. According to the results presented here, studies focusing on establishing trace element proxy

438 transfer functions could benefit from basing their regressions on total shell trace element concentrations

439 rather than measurements in the shell hinge in their attempts to isolate environmental controls on trace

440 element concentrations in bivalve calcite.

441

442 **Code availability**

443 The R script of the ShellTrace model used in this paper was published in the open source research data

444 repository Zenodo (http://doi.org/10.5281/zenodo.817258). The complete script used for the ShellTrace

445 model in this publication will be made available by means of an R package in the CRAN repository

446 (https://cran.r-project.org), and the script is given in **supplementary data 2**.

447

448 **Acknowledgments**

455

456 **References**

457 Affek, H.P., Bar-Matthews, M., Ayalon, A., Matthews, A., Eiler, J.M., 2008. Glacial/interglacial temperature variations in Soreq cave
458   speleothems as recorded by "clumped isotope"thermometry. Geochimica et Cosmochimica Acta 72, 5351–5360.
459 Andrews, T., Gregory, J.M., Webb, M.J., Taylor, K.E., 2012. Forcing, feedbacks and climate sensitivity in CMIP5 coupled atmosphere-
460   ocean climate models. Geophysical Research Letters 39.
461 Bachelet, G., 1980. Growth and recruitment of the tellinid bivalve Macoma balthica at the southern limit of its geographical distribution, the
462   Gironde estuary (SW France). Marine Biology 59, 105–117.
463 Barron, E.J., Washington, W.M., 1984. The role of geographic variables in explaining paleoclimates: Results from Cretaceous climate
464   model sensitivity studies. Journal of Geophysical Research: Atmospheres 89, 1267–1279.
465 Bartol, I.K., Mann, R., Luckenbach, M., 1999. Growth and mortality of oysters (Crassostrea virginica) on constructed intertidal reefs: effects
466   of tidal height and substrate level. Journal of Experimental Marine Biology and Ecology 237, 157–184.
467 Beniash, E., Ivanina, A., Lieb, N.S., Kurochkin, I., Sokolova, I.M., 2010. Elevated level of carbon dioxide affects metabolism and shell
468   formation in oysters Crassostrea virginica. Marine Ecology Progress Series 419, 95–108.
469 Carré, M., Bentaleb, I., Bruguier, O., Ordinola, E., Barrett, N.T., Fontugne, M., 2006. Calcification rate influence on trace element
470   concentrations in aragonitic bivalve shells: evidences and mechanisms. Geochimica et Cosmochimica Acta 70, 4906–4920.
471 Carriker, M.R., Palmer, R.E., Sick, L.V., Johnson, C.C., 1980. Interaction of mineral elements in sea water and shell of oysters (Crassostrea
472   virginica (Gmelin)) cultured in controlled and natural systems. Journal of experimental marine biology and ecology 46, 279–296.
473 Claussen, M., Mysak, L., Weaver, A., Crucifix, M., Fichefet, T., Loutre, M.-F., Weber, S., Alcamo, J., Alexeev, V., Berger, A., others,
474   2002. Earth system models of intermediate complexity: closing the gap in the spectrum of climate system models. Climate
475   dynamics 18, 579–586.
476 Côté, J., Himmelman, J.H., Claereboudt, M.R., 1994. Separating effects of limited food and space on growth of the giant scallop
477   Placopecten magellanicus in suspended culture. MARINE ECOLOGY-PROGRESS SERIES 106, 85–85.
478 Currey, J.D., Taylor, J.D., 1974. The mechanical behaviour of some molluscan hard tissues. Journal of Zoology 173, 395–406.
479 de Winter, N.J., Claeys, P., 2016. Micro X-ray fluorescence (μXRF) line scanning on Cretaceous rudist bivalves: A new method for
480   reproducible trace element profiles in bivalve calcite. Sedimentology. doi:10.1111/sed.12299
481 de Winter, N., Sinnesael, M., Makarona, C., Vansteenberge, S., Claeys, P., 2017. Trace element analyses of carbonates using portable and
482   micro-X-ray fluorescence: Performance and optimization of measurement parameters and strategies. Journal of Analytical
483   Atomic Spectrometry 32, 1211-1223.
484 de Winter, N.J., Goderis, S., Dehairs, F., Jagt, J.W.M., Fraaije, R.H.B., Van Malderen, S.J.M., Vanhaecke, F., Claeys, P., Tropical
485   seasonality in the late Campanian (Late Cretaceous): Comparison between multiproxy records from three bivalve taxa from
486   Oman. Palaeogeography, Palaeoclimatology, Palaeoecology, in review.

487 Diederich, S., 2006. High survival and growth rates of introduced Pacific oysters may cause restrictions on habitat use by native mussels in
488   the Wadden Sea. Journal of Experimental Marine Biology and Ecology 328, 211–227.
489 Edwards, M., John, A.W.G., Johns, D.G., Reid, P.C., 2001. Case history and persistence of the non-indigenous diatom Coscinodiscus
490   wailesii in the north-east Atlantic. Journal of the Marine Biological Association of the UK 81, 207–211.
491 Freitas, P.S., Clarke, L.J., Kennedy, H., Richardson, C.A., Abrantes, F., 2006. Environmental and biological controls on elemental (Mg/Ca,
492   Sr/Ca and Mn/Ca) ratios in shells of the king scallop Pecten maximus. Geochimica et Cosmochimica Acta 70, 5119–5133.
493 Freitas, P.S., Clarke, L.J., Kennedy, H., Richardson, C.A., others, 2009. Ion microprobe assessment of the heterogeneity of Mg/Ca, Sr/Ca
494   and Mn/Ca ratios in Pecten maximus and Mytilus edulis (bivalvia) shell calcite precipitated at constant temperature.
495   Biogeosciences Discussions 6, 1267.
496 Füllenbach, C.S., Schöne, B.R., Mertz-Kraus, R., 2015. Strontium/lithium ratio in aragonitic shells of Cerastoderma edule (Bivalvia)—A
497   new potential temperature proxy for brackish environments. Chemical Geology 417, 341–355.
498 Galtsoff, P.S., 1964. The American Oyster: US Fish and Wildlife Service. Fishery Bulletin 64, 480.
499 Gillikin, D.P., Lorrain, A., Bouillon, S., Willenz, P., Dehairs, F., 2006. Stable carbon isotopic composition of Mytilus edulis shells: relation
500   to metabolism, salinity, δ 13 C DIC and phytoplankton. Organic Geochemistry 37, 1371–1382.
501 Gillikin, D.P., Lorrain, A., Navez, J., Taylor, J.W., André, L., Keppens, E., Baeyens, W., Dehairs, F., 2005. Strong biological controls on
502   Sr/Ca ratios in aragonitic marine bivalve shells. Geochemistry, Geophysics, Geosystems 6.
503 Gillikin, D.P., Lorrain, A., Paulet, Y.-M., André, L., Dehairs, F., 2008. Synchronous barium peaks in high-resolution profiles of calcite and
504   aragonite marine bivalve shells. Geo-Marine Letters 28, 351–358.
505 Goodwin, D.H., Flessa, K.W., Schöne, B.R., Dettman, D.L., 2001. Cross-calibration of daily growth increments, stable isotope variation,
506   and temperature in the Gulf of California bivalve mollusk Chione cortezi: implications for paleoenvironmental analysis. Palaios
507   16, 387–398.
508 Goreau, T.J., 1977. Coral skeletal chemistry: physiological and environmental regulation of stable isotopes and trace metals in Montastrea
509   annularis. Proceedings of the Royal Society of London B: Biological Sciences 196, 291–315.
510 Hart, D.R., Chute, A.S., 2009. Verification of Atlantic sea scallop (Placopecten magellanicus) shell growth rings by tracking cohorts in
511   fishery closed areas. Canadian Journal of Fisheries and Aquatic Sciences 66, 751–758.
512 Hesselbo, S.P., Gröcke, D.R., Jenkyns, H.C., Bjerrum, C.J., Farrimond, P., Bell, H.S.M., Green, O.R., 2000. Massive dissociation of gas
513   hydrate during a Jurassic oceanic anoxic event. Nature 406, 392–395.
514 Huber, B.T., Hodell, D.A., Hamilton, C.P., 1995. Middle–Late Cretaceous climate of the southern high latitudes: stable isotopic evidence for
515   minimal equator-to-pole thermal gradients. Geological Society of America Bulletin 107, 1164–1191.
516 Immenhauser, A., Nägler, T.F., Steuber, T., Hippler, D., 2005. A critical assessment of mollusk 18O/16O, Mg/Ca, and 44Ca/40Ca ratios as
517   proxies for Cretaceous seawater temperature seasonality. Palaeogeography, Palaeoclimatology, Palaeoecology 215, 221–237.
518   doi:10.1016/j.palaeo.2004.09.005
519 Kerswill, C.J., 1949. Effects of water circulation on the growth of quahaugs and oysters. Journal of the Fisheries Board of Canada 7, 545–
520   551.
521 Kirby, M.X., Soniat, T.M., Spero, H.J., 1998. Stable isotope sclerochronology of Pleistocene and Recent oyster shells (Crassostrea
522   virginica). Palaios 13, 560–569.
523 Klein, R.T., Lohmann, K.C., Thayer, C.W., 1996a. Bivalve skeletons record sea-surface temperature and δ18O via Mg/Ca and 18O/16O
524   ratios. Geology 24, 415–418.
525 Klein, R.T., Lohmann, K.C., Thayer, C.W., 1996b. SrCa and 13C12C ratios in skeletal calcite of Mytilus trossulus: Covariation with
526   metabolic rate, salinity, and carbon isotopic composition of seawater. Geochimica et Cosmochimica Acta 60, 4207–4221.
527 Klein, R.T., Lohmann, K.C., Kennedy, G.L., 1997. Elemental and isotopic proxies of paleotemperature and paleosalinity: Climate
528   reconstruction of the marginal northeast Pacific ca. 80 ka. Geology 25, 363–366.
529 Kutzbach, J.E., Guetter, P.J., Ruddiman, W.F., Prell, W.L., 1989. Sensitivity of climate to late Cenozoic uplift in Southern Asia and the
530   American West: Numerical experiments. Journal of Geophysical Research: Atmospheres 94, 18393–18407.
531 Lazareth, C.E., Vander Putten, E., André, L., Dehairs, F., 2003. High-resolution trace element profiles in shells of the mangrove bivalve
532   Isognomon ephippium: a record of environmental spatio-temporal variations? Estuarine, Coastal and Shelf Science 57, 1103–
533   1114.
534 Lee, S.W., Kim, Y.M., Kim, R.H., Choi, C.S., 2008. Nano-structured biogenic calcite: A thermal and chemical approach to folia in oyster
535   shell. Micron 39, 380–386. doi:10.1016/j.micron.2007.03.006
536 Leng, M.J., Marshall, J.D., 2004. Palaeoclimate interpretation of stable isotope data from lake sediment archives. Quaternary Science
537   Reviews 23, 811–831.
538 Lorrain, A., Gillikin, D.P., Paulet, Y.-M., Chauvaud, L., Le Mercier, A., Navez, J., André, L., 2005. Strong kinetic effects on Sr/Ca ratios in
539   the calcitic bivalve Pecten maximus. Geology 33, 965–968.
540 MacDonald, B.A., Thompson, R.J., 1985. Influence of temperature and food availability on the ecological energetics of the giant scallop
541   Placopecten magellanicus. I. Growth rates of shell and somatic tissue. Marine ecology progress series. Oldendorf 25, 279–294.
542 McDermott, F., 2004. Palaeo-climate reconstruction from stable isotope variations in speleothems: a review. Quaternary Science Reviews
543   23, 901–918.
544 Palmer, R.E., Carriker, M.R., 1979. Effects of cultural conditions on morphology of the shell of the oyster Crassostrea virginica, in:
545   Proceedings of the National Shellfisheries Association. pp. 58–72.
546 R Core Team, 2013. R: A language and environment for statistical computing. R Foundation for Statistical Computing. Vienna, Austria.
547 Reinfelder, J.R., Wang, W.-X., Luoma, S.N., Fisher, N.S., 1997. Assimilation efficiencies and turnover rates of trace elements in marine
548   bivalves: a comparison of oysters, clams and mussels. Marine Biology 129, 443–452.
549 Richardson, C.A., Peharda, M., Kennedy, H., Kennedy, P., Onofri, V., 2004a. Age, growth rate and season of recruitment of Pinna nobilis
550   (L) in the Croatian Adriatic determined from Mg: Ca and Sr: Ca shell profiles. Journal of Experimental Marine Biology and
551   Ecology 299, 1–16.
552 Richardson, C.A., Peharda, M., Kennedy, H., Kennedy, P., Onofri, V., 2004b. Age, growth rate and season of recruitment of Pinna nobilis
553   (L) in the Croatian Adriatic determined from Mg: Ca and Sr: Ca shell profiles. Journal of Experimental Marine Biology and
554   Ecology 299, 1–16.
555 Schöne, B., Tanabe, K., Dettman, D.L., Sato, S., 2003. Environmental controls on shell growth rates and d 18 O of the shallow-marine
556   bivalve mollusk Phacosoma japonicum in Japan. Marine Biology 142, 473–485.
557 Schöne, B.R., Zhang, Z., Radermacher, P., Thébault, J., Jacob, D.E., Nunn, E.V., Maurer, A.-F., 2011. Sr/Ca and Mg/Ca ratios of
558   ontogenetically old, long-lived bivalve shells (Arctica islandica) and their function as paleotemperature proxies.
559   Palaeogeography, Palaeoclimatology, Palaeoecology 302, 52–64.
560 Sluijs, A., Schouten, S., Pagani, M., Woltering, M., Brinkhuis, H., Damsté, J.S.S., Dickens, G.R., Huber, M., Reichart, G.-J., Stein, R.,
561   others, 2006. Subtropical Arctic Ocean temperatures during the Palaeocene/Eocene thermal maximum. Nature 441, 610–613.

Geoscientific
Model Development
Discussions

562   Stenzel, H.B., 1963. Aragonite and calcite as constituents of adult oyster shells. Science 142, 232–233.
563   Steuber, T., 1999. Isotopic and chemical intra-shell variations in low-Mg calcite of rudist bivalves (Mollusca-Hippuritacea): disequilibrium
564   fractionations and late Cretaceous seasonality. International Journal of Earth Sciences 88, 551–570.
565   Surge, D., Lohmann, K.C., 2008. Evaluating Mg/Ca ratios as a temperature proxy in the estuarine oyster, Crassostrea virginica. Journal of
566   Geophysical Research: Biogeosciences 113.
567   Surge, D., Lohmann, K.C., Dettman, D.L., 2001. Controls on isotopic chemistry of the American oyster, Crassostrea virginica: implications
568   for growth patterns. Palaeogeography, Palaeoclimatology, Palaeoecology 172, 283–296.
569   Takesue, R.K., van Geen, A., 2004. Mg/Ca, Sr/Ca, and stable isotopes in modern and Holocene Protothaca staminea shells from a northern
570   California coastal upwelling region. Geochimica et Cosmochimica Acta 68, 3845–3861.
571   Titschack, J., Zuschin, M., Spötl, C., Baal, C., 2010. The giant oyster Hyotissa hyotis from the northern Red Sea as a decadal-scale archive
572   for seasonal environmental fluctuations in coral reef habitats. Coral Reefs 29, 1061–1075.
573   Ullmann, C.V., Böhm, F., Rickaby, R.E., Wiechert, U., Korte, C., 2013. The Giant Pacific Oyster (Crassostrea gigas) as a modern analog for
574   fossil ostreoids: isotopic (Ca, O, C) and elemental (Mg/Ca, Sr/Ca, Mn/Ca) proxies. Geochemistry, Geophysics, Geosystems 14,
575   4109–4120.
576   Ullmann, C.V., Frei, R., Korte, C., Lüter, C., 2017. Element/Ca, C and O isotope ratios in modern brachiopods: Species-specific signals of
577   biomineralization. Chemical Geology.
578   Ullmann, C.V., Wiechert, U., Korte, C., 2010. Oxygen isotope fluctuations in a modern North Sea oyster (Crassostrea gigas) compared with
579   annual variations in seawater temperature: Implications for palaeoclimate studies. Chemical Geology 277, 160–166.
580   Urban, H.-J., 2000. Culture potential of the pearl oyster (Pinctada imbricata) from the Caribbean.: I. Gametogenic activity, growth, mortality
581   and production of a natural population. Aquaculture 189, 361–373.
582   Vermeij, G.J., 2014. The oyster enigma variations: a hypothesis of microbial calcification. Paleobiology 40, 1–13.
583   Vihtakari, M., Ambrose, W.G., Renaud, P.E., Locke, W.L., Carroll, M.L., Berge, J., Clarke, L.J., Cottier, F., Hop, H., 2017. A key to the
584   past? Element ratios as environmental proxies in two Arctic bivalves. Palaeogeography, Palaeoclimatology, Palaeoecology 465,
585   316–332.
586   Von Bertalanffy, L., 1957. Quantitative laws in metabolism and growth. The quarterly review of biology 32, 217–231.
587   Wanamaker Jr, A.D., Kreutz, K.J., Wilson, T., Borns Jr, H.W., Introne, D.S., Feindel, S., 2008. Experimentally determined Mg/Ca and
588   Sr/Ca ratios in juvenile bivalve calcite for Mytilus edulis: implications for paleotemperature reconstructions. Geo-Marine Letters
589   28, 359–368.
590   Wang, W.-X., Fisher, N.S., 1996. Assimilation of trace elements and carbon by the mussel Mytilus edulis: effects of food composition.
591   Limnology and Oceanography 4, l.
592   Wang, Y.-J., Cheng, H., Edwards, R.L., An, Z.S., Wu, J.Y., Shen, C.-C., Dorale, J.A., 2001. A high-resolution absolute-dated late
593   Pleistocene monsoon record from Hulu Cave, China. Science 294, 2345–2348.
594   Wiltshire, K.H., Malzahn, A., Greve, W., Wirtz, K., Janisch, S., Mangelsdorf, P., Manly, B.F., Boersma, M., 2008. Resilience of North Sea
595   phytoplankton spring blooms dynamics: an analysis of long term data at Helgoland Roads. Limnology and Oceanography 53,
596   1294–1302.
597   Zachos, J., Pagani, M., Sloan, L., Thomas, E., Billups, K., 2001. Trends, rhythms, and aberrations in global climate 65 Ma to present.
598   Science 292, 686–693.
599   Zachos, J.C., Schouten, S., Bohaty, S., Quattlebaum, T., Sluijs, A., Brinkhuis, H., Gibbs, S.J., Bralower, T.J., 2006. Extreme warming of
600   mid-latitude coastal ocean during the Paleocene-Eocene Thermal Maximum: Inferences from TEX86 and isotope data. Geology
601   34, 737–740.

602

603   **FIGURE 1:** Schematic overview of the growth model and trace element module described in this paper. Yellow

604   boxes indicate the modelling steps (Step 1-6) described in chapter 3, diamond-shaped elements represent data

605   packages, ellipses represent model input parameters and boxes represent functions in the model. Elements

606   are connected by arrows if they interact (i.e. if data packages and/or model parameters serve as input or

607   output of model functions). Coloured data packages are the output of the model.

608   **FIGURE 2:** Example of a colour scan (top), a µXRF phase map (middle) and the digitized increments (bottom) of

609   a *Crassostrea gigas* shell. Phase maps show the distribution of Araldite® 2020 resin (red), foliated calcite

610   (green), chalky calcite (blue) and detrital material (yellow) in the shell cross sections. The *C. gigas* shell

611   depicted in this figure corresponds to *C. gigas* shell #1 in **Table 2**.

612   **FIGURE 3:** Schematic illustration of morphology of a typical bivalve shell including an indication of all

613   parameters used in the growth and trace element models. **Figure 2A** shows a cross section along the shell's

614   major growth axis (XY plane), which is the plane along which the shells were sectioned. This cross section

615   illustrates the parameters used to define shell increments and how interpolation between them is done (see

616   section 3.1, model step 2). **Figure 2B** shows an overview of the shell and a definition of the axes (X, Y and Z) as

617   well as the parameters defined in the base ellipse of the shell (see section 3.1, model step 3). **Figure 2C** shows

618   a perpendicular cross section through the width of the shell (YZ plane), which illustrates the parameters used

619   in the determination of shell volume (see section 3.1, model step 4).

620   **FIGURE 4:** Overview of the results of quantitative XRF line scanning on a *C. gigas* shell (#1 in **Table 2**). On top of

621   the figure is a colour scan of a cross section through the shell. The enlarged image on the left hand side shows

622   the shell hinge including digitized growth increments (black lines with increment numbers), annual chronology

623   interpreted from trace element records (yellow and transparent bands with years) and the location of the line

624   scan (A to B, dark blue arrow). The lower right graph shows results of trace element records along the XRF line

625   scan with growth increments (black lines) and annual chronology (yellow and transparent areas) indicated

626   vertically on the graphs. From top to bottom, records of Ca (dark blue), Si (dark red), Zn (magenta), Mn

627   (purple), Fe (orange), S (red), Mg (green) and Sr (blue) are plotted against line scan distance, increment

628   number and time on three separate x-axes at the bottom of the graph.

629   **FIGURE 5:** Graphs showing modelled evolution of shell length (top left), average shell thickness (bottom left),

630   shell volume and mass (top right) and shell growth rates (bottom right) with shell age. Solid blue lines in

631   different shadings indicate records from individual *C. gigas* shells. Thin dashed blue curves indicate models

632   fitted through the growth curves of *C. gigas* shells, while bold dashed black curves show models fitted through

633   a composite of modelled data from all shells combined. Regression formulae and statistics are given in **Table 2**.

634   **FIGURE 6:** Plotted results of trace element modelling and line scanning in one of the *C. gigas* shells (#1 in **Table**

635   **2**). Shaded areas indicate the evolution of modelled accumulation rates (in mg/yr) of major and trace elements

636   with shell age. Solid coloured lines indicate the change in modelled total shell concentrations with shell age.

637   Coloured points connected by black lines indicate measured elemental concentrations in the hinge of the

638   shells plotted against shell age (see also **Figure 4**)

639   **TABLE 1:** Table listing all functions used in the growth and trace element models (see chapter 3) and the

640   variables used in these functions. Function names and names of data packages are also found in **Figure 1** and

641   in the text.

642   **TABLE 2:** Overview of measured shell dimensions (top left), dimensions of XRF maps of all shells used in this

643   study (top right), shell dimensions at the end of the model run (bottom left) and parameters of growth curves

644   fitted through the modelled data (bottom right). Average density of shells was calculated from the averages of

645   shell mass and volume.

646   **TABLE 3:** Table listing concentrations of all elements used in this study in both chalky and foliated calcite

647   phases of *C. gigas* and *O. figari* shells. The "% of map"-column shows the amount of pixels the mineral phases

648   take up relative to the total cross section area (not including resin mapped in the XRF mapping, see **Figure 3**).

649 **Supplementary data 1**: SVG and CSV files of cross sections through all the *Crassostrea gigas* shells used in this
650 study

651 **Supplementary data 2**: Complete R-script used to model growth and trace element uptake as described in this
652 study

653 **Supplementary data 3**: Data of phase analysis of all trace element XRF maps including RGB colour values and
654 trace element concentrations of all phases.

655 **Supplementary data 4**: Repository containing all data matrices generated by the model ran on all shells
656 featuring in this study.

657 **Supplementary data 5**: BMP images of phase maps of all shell cross sections used as input of the trace
658 element model in this study.

Geoscientific
Model Development
Discussions

Figure 1

Geoscientific
Model Development
Discussions

Figure 2

Figure 3

Figure 4

Geoscientific
Model Development
Discussions

Figure 5

Figure 6

Geoscientific Model Development Discussions — Open Access EGU
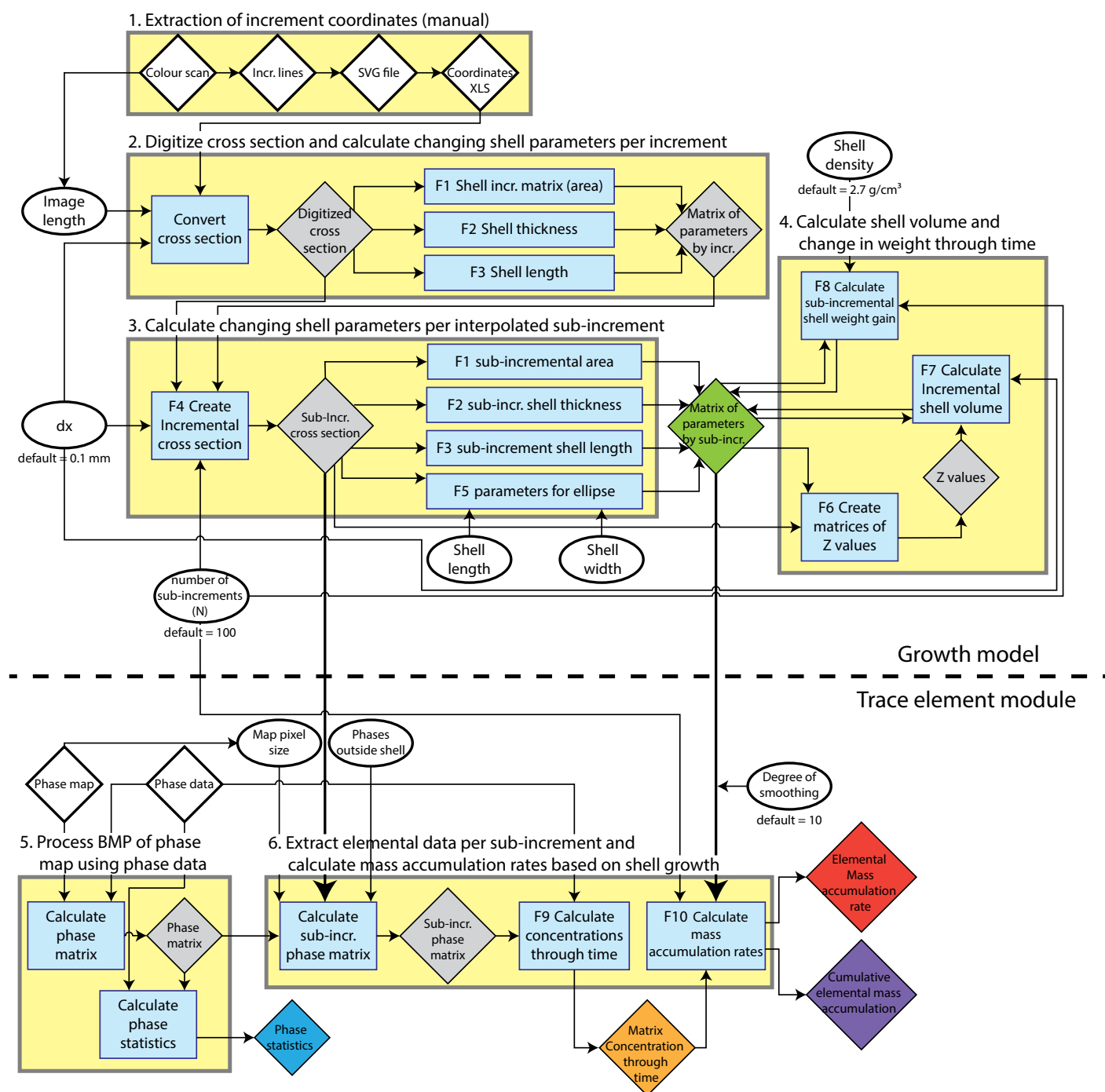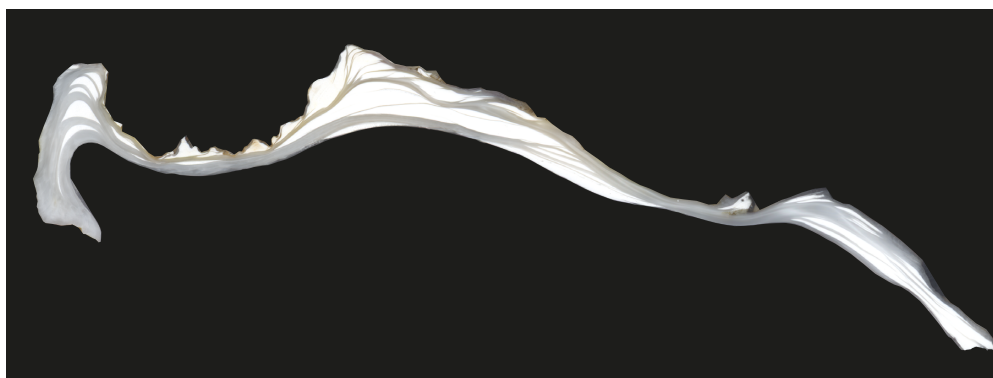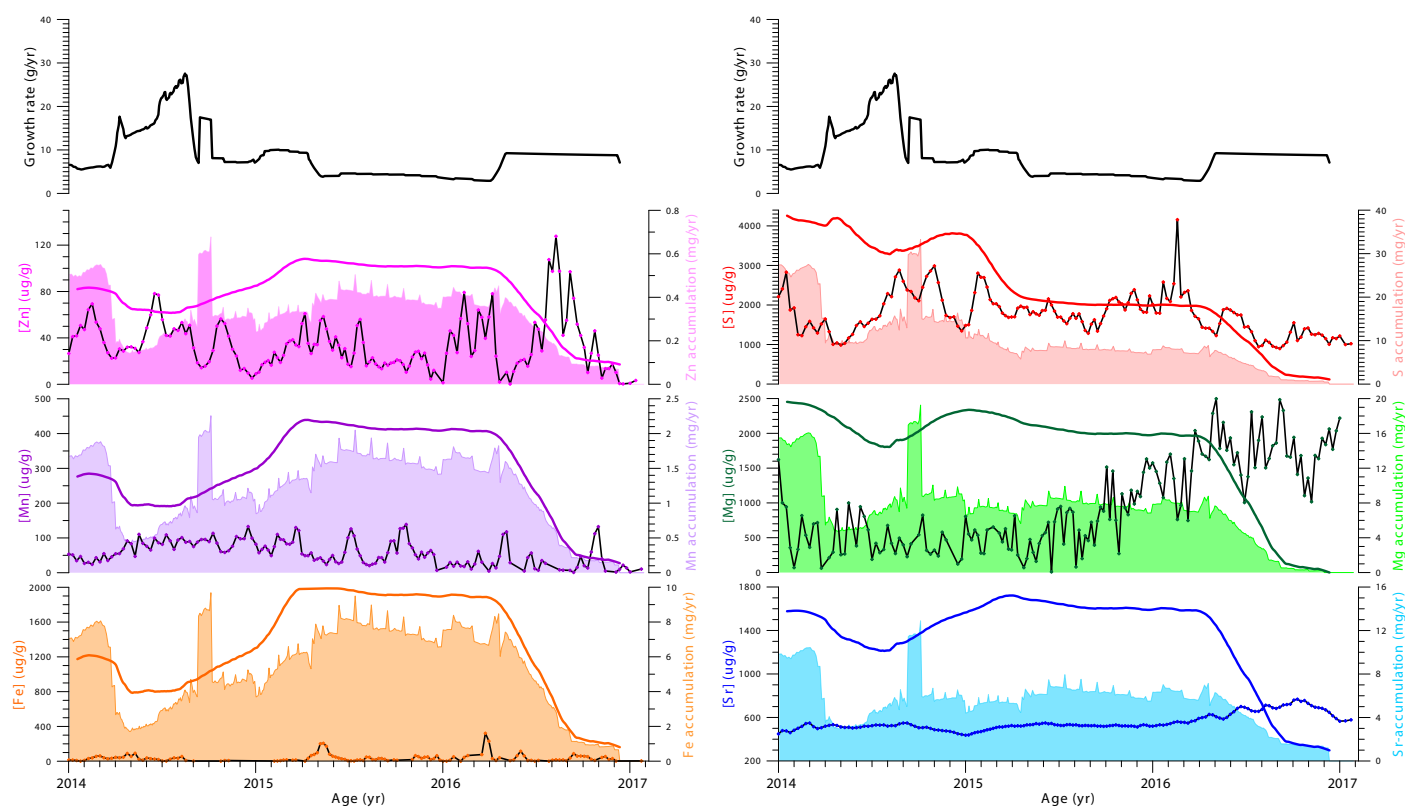
Table 1

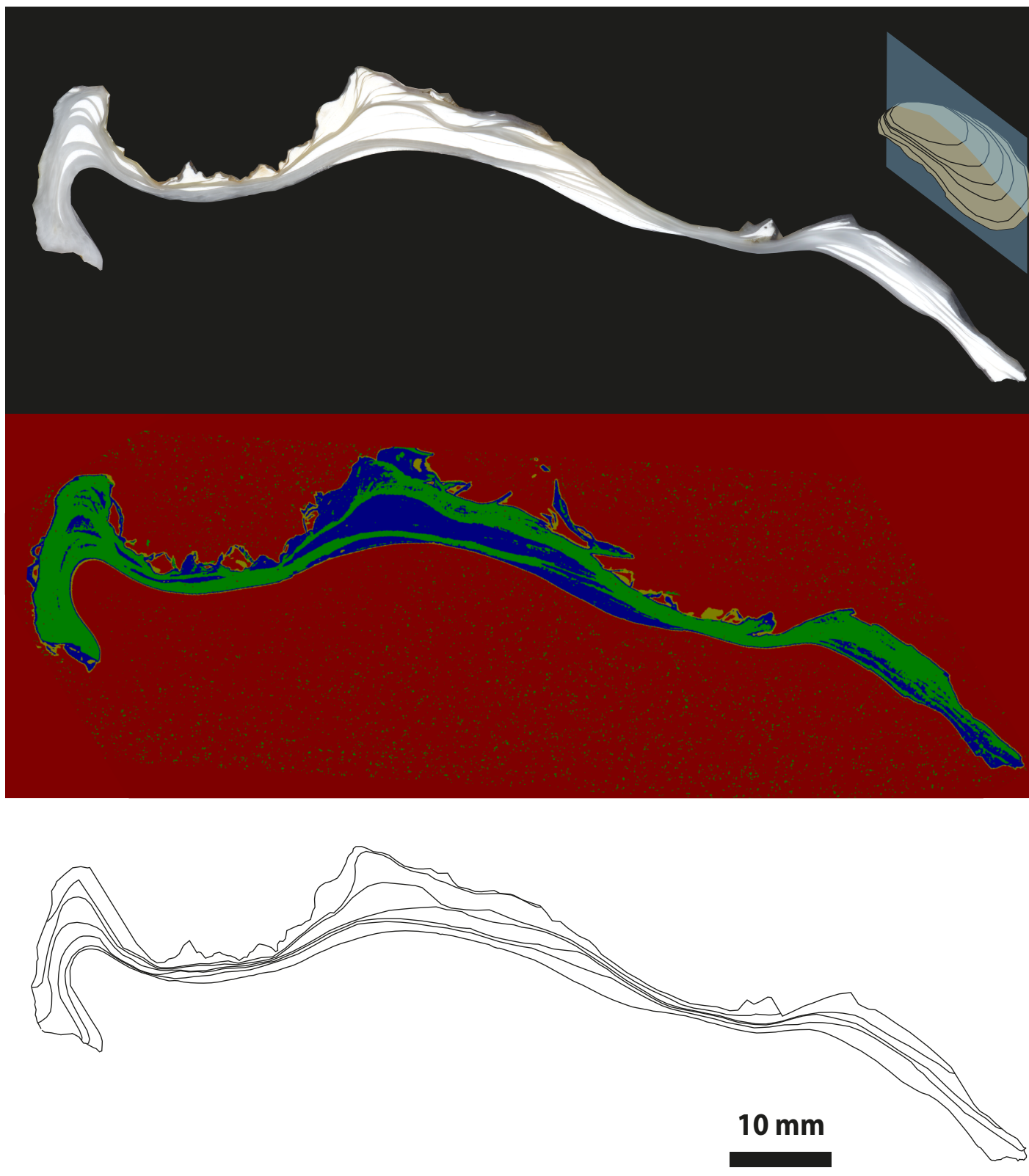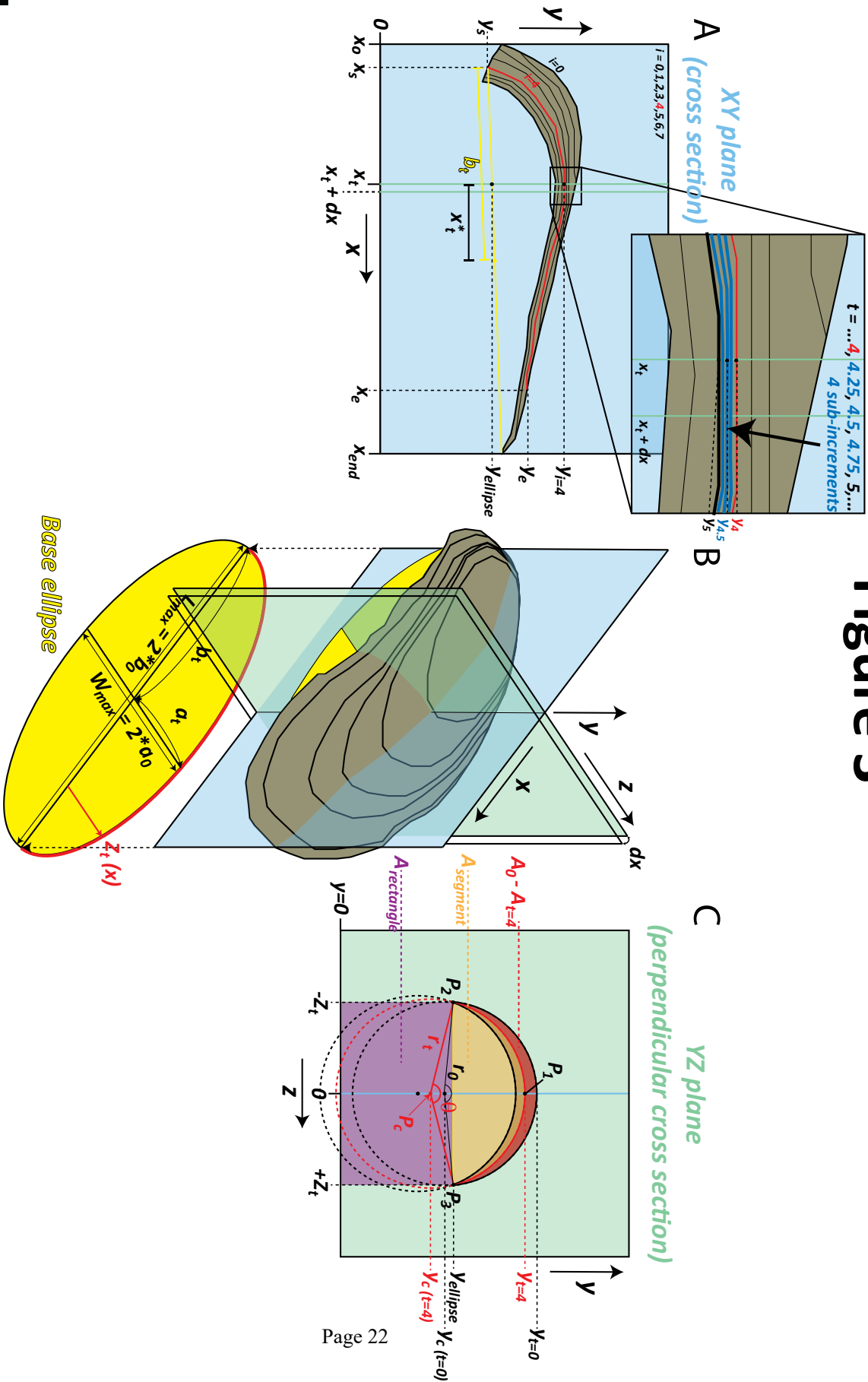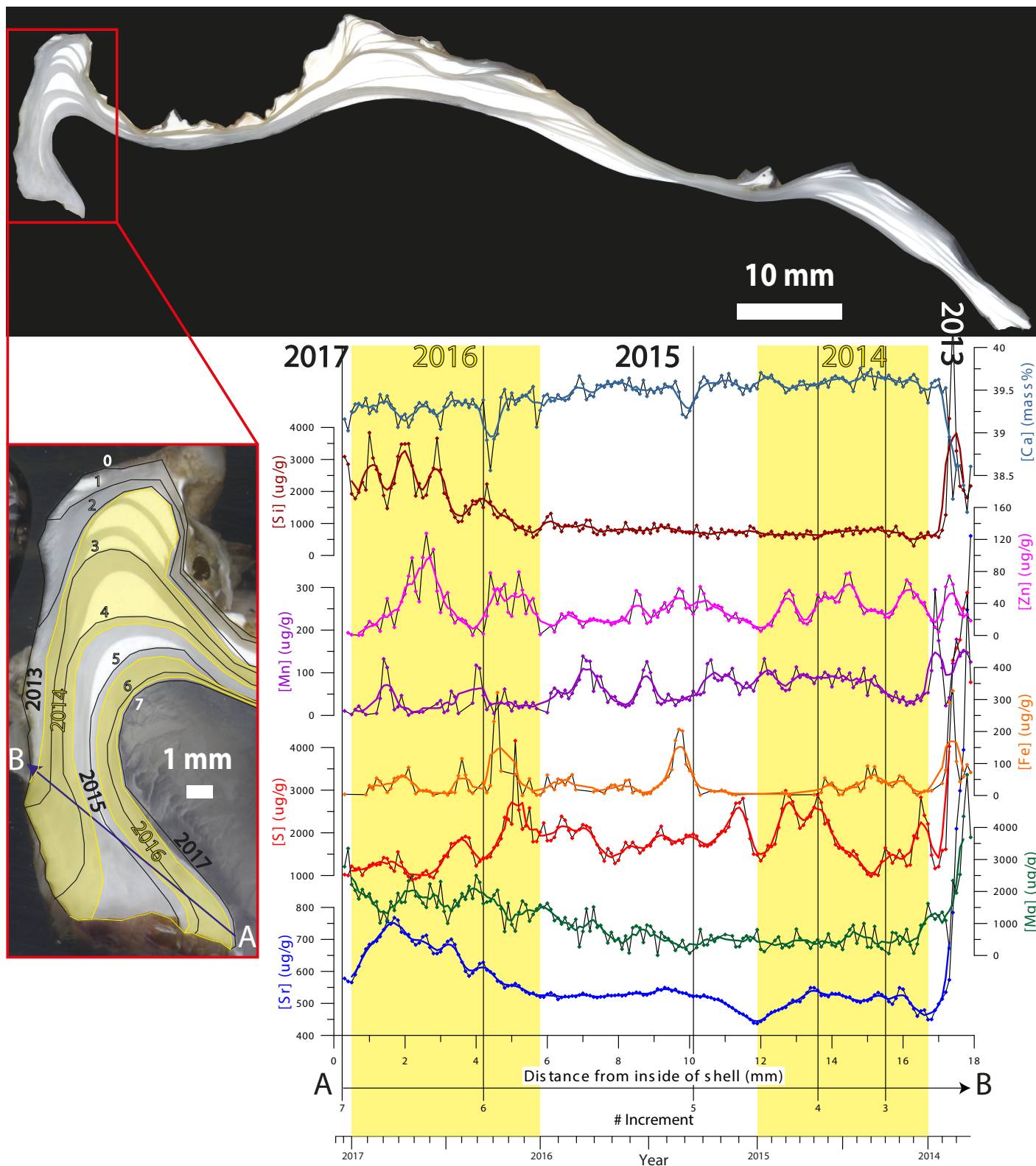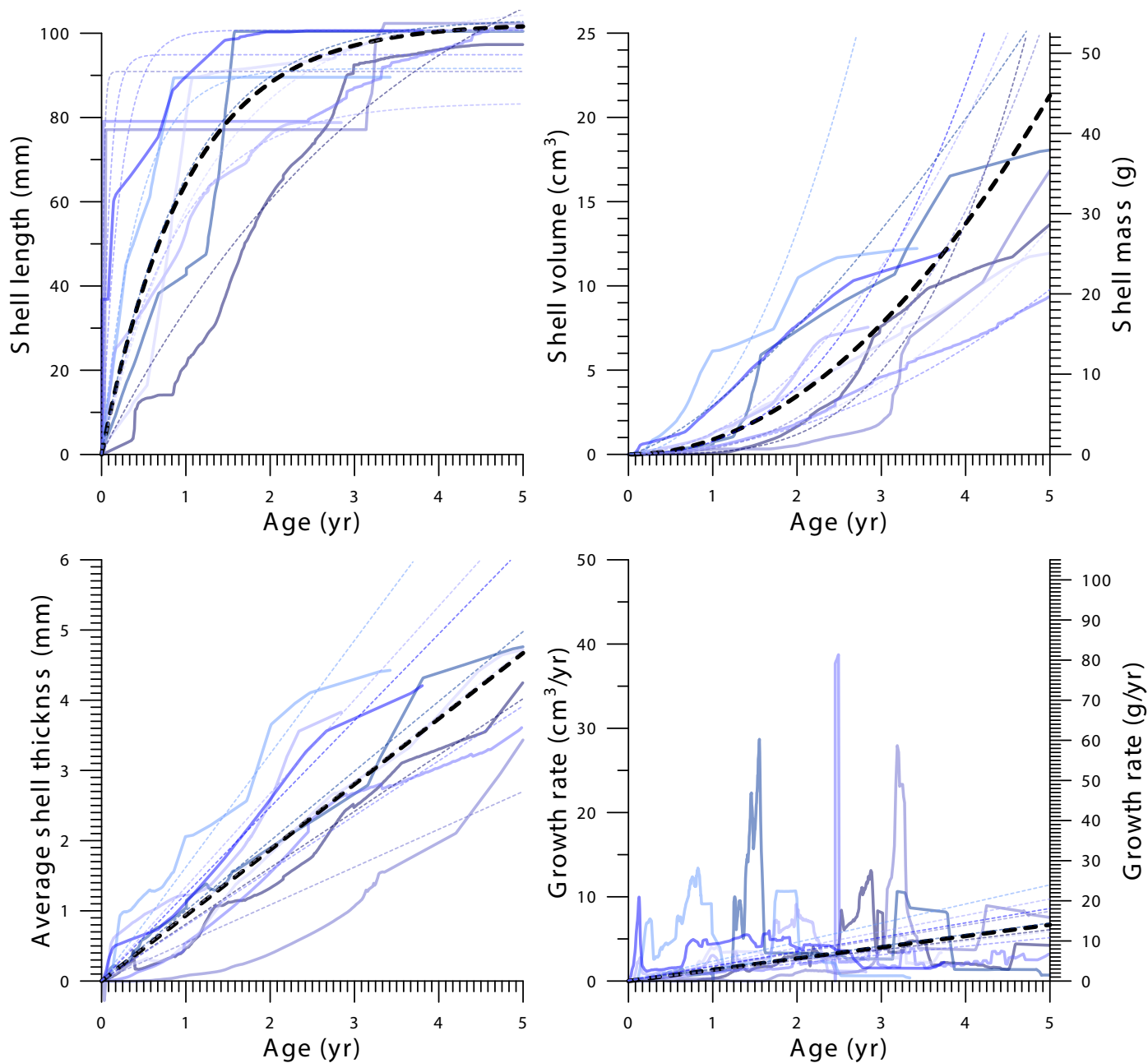| Model	Model step	Function name	Equation	variables IN	source of variables	variables OUT	variables stored in:
Growth model	Step 2	F1	$O_i = \int_{x_0}^{x_{end}} Y_{i-1}(x) - Y_i(x)\, dx$	x_0	Digitized cross section	A_i	Matrix of parameters by increment
				x_{end}	Digitized cross section		
				$Y_i(x)$	Digitized cross section		
				$Y_{i-1}(x)$	Digitized cross section		
				dx	dx		
		F2	$T_i = \frac{\sum_{x_0}^{x_{end}} Y_0(x) - Y_i(x)}{x_{end} - x_0}$	x_0	Digitized cross section	T_i	Matrix of parameters by increment
				x_{end}	Digitized cross section		
				$Y_i(x)$	Digitized cross section		
				$Y_{i-1}(x)$	Digitized cross section		
		F3	$L_i = \sqrt{(x_e - x_s)^2 + (Y_e - Y_s)^2}$	x_e	Digitized cross section	L_i	Matrix of parameters by increment
				x_s	Digitized cross section		
				Y_e	Digitized cross section		
				Y_s	Digitized cross section		
	Step 3	F4 — F4.1	$\left[\left[Y_t(x) = Y_{i-1}(x) - \frac{n}{N} * (Y_{i-1}(x) - Y_i(x))\right]_{n=0}^{n=N-1}\right]_{x=x_0}^{x=x_{end}}$	$Y_i(x)$	Digitized cross section	$Y_t(x)$	Sub-incremental cross section
				$Y_{i-1}(x)$	Digitized cross section		
		F4.2	$t = i - 1 + \frac{n}{N}$	N	Number of sub-increments		
		F5 — F5.1	$a_t = \frac{1}{2} * \frac{W_{max}}{L_{max}} * (x_e - x_s)$	W_{max}	Shell width	a_t	Matrix of parameters by sub-increment
				L_{max}	Shell length		
				x_e	Sub-incremental cross section		
				x_s	Sub-incremental cross section		
		F5.2	$b_t = \frac{1}{2} * (x_e - x_s)$	x_e	Sub-incremental cross section	b_t	Matrix of parameters by sub-increment
				x_s	Sub-incremental cross section		
	Step 4	F6 — F6.1	$\left(\frac{Z_t(x)}{a_t}\right)^2 + \left(\frac{x^*_t}{b_t}\right)^2 = 1$	a_t	Matrix of parameters by sub-increment	$Z_t(x)$	Z-values
		F6.2	$Z_t(x) = \left(\frac{a_t}{b_t}\right) * \sqrt{b_t^2 - x^*_t{}^2}$	b_t	Matrix of parameters by sub-increment		
		F6.3	$x^*_t = x - x_s - b_t$	x	Sub-incremental cross section		
				x_s	Sub-incremental cross section		
		F7 — F7.1	$V_t = \int_{x_0}^{x_{end}} (A_0(x) - A_t(x)) dx$	x_0	Sub-incremental cross section	V_t	Matrix of parameters by sub-increment
				x_{end}	Sub-incremental cross section		
				dx	dx		
		F7.2	$Y_{ellipse} = Y_s + \left(\frac{Y_e - Y_s}{x_e - x_s}\right) * (x - x_s)$	Y_s	Sub-incremental cross section		
				Y_e	Sub-incremental cross section		
		F7.3	$\Delta y^2 + \Delta z^2 = r^2$	x_s	Sub-incremental cross section		
		F7.4	$(y_1 - y_c)^2 + (z_1 - z_c)^2 = (y_3 - y_c)^2 + (z_3 - z_c)^2$	x_e	Sub-incremental cross section		
		F7.5	$(Y_t(x) - Y_c(x))^2 + (0 - 0)^2 = (Y_{ellipse}(x) - Y_c(x))^2 + (Z_t(x) - 0)^2$				
		F7.6	$Y_c(x) = \frac{(Y_t(x)^2 - Y_{ellipse}(x)^2 - Z_t(x)^2)}{2 * (Y_t(x) - Y_{ellipse}(x))}$	x	Matrix of parameters by sub-increment		
		F7.7	$r_t(x) = \sqrt{Z_t(x)^2 + (Y_{ellipse}(x) - Y_c(x))^2}$	$Y_t(x)$	Matrix of parameters by sub-increment		
		F7.8	$\theta = 2 * \sin^{-1}\left(\frac{Z_t(x)}{r_t(x)}\right)$				
		F7.9	$A_t = \begin{cases} A_{segment} + A_{rectangle} = \frac{1}{2}(r_t(x))^2 * (\theta - \sin\theta) + 2 * Z_t(x) * Y_{ellipse}(x), & Y_t(x) \geq Y_{ellipse}(x) \\ A_{rectangle} - A_{segment} = 2 * Z_t(x) * Y_{ellipse}(x) - \frac{1}{2}(r_t(x))^2 * (\theta - \sin\theta), & Y_t(x) < Y_{ellipse}(x) \end{cases}$	$Z_t(x)$	Z-values		
		F8 — F8.1	$\Delta M_t = \rho * (V_{t-1} - V_t)$	V_t	Matrix of parameters by sub-increment	ΔM_t	Matrix of parameters by sub-increment
				V_{t-1}	Matrix of parameters by sub-increment		
		F8.2	$M_t = \rho * V_t$	ρ	Shell density	M_t	Matrix of parameters by sub-increment
Trace element model	Step 6	F9	$C_t^E = \sum_{p=p_1}^{p=p_n} \frac{S_p}{S_{tot}} * C_p^E \qquad p \text{ in } [p_1, p_2, p_3, \ldots, p_n]$	S_p	Sub-increment phase matrix	C_t^E	Matrix of concentration through time
				S_{tot}	Sub-increment phase matrix		
				C_p^E	Phase data		
		F10 — F10.1	$M_t^E = C_t^E * M_t$	C_t^E	Matrix of concentration through time	M_t^E	Cumulative elemental mass accumulation matrix
				M_t	Matrix of parameters by sub-increment		
		F10.2	$\left[\frac{\partial M}{\partial t}\right]_t^E = C_t^E * N * \Delta M_t$	ΔM_t	Matrix of parameters by sub-increment	$\left[\frac{\partial M}{\partial t}\right]_t^E$	Elemental mass accumulation rate matrix
				N	Number of sub-increments		

Geoscientific Model Development Discussions — Open Access — EGU

Table 2

Oyster dimensions

#	Shell length (mm)	Shell width (mm)	Maximum shell thickness (mm)	Shell mass (g)	Shell volume (cm3)	Density
Crassostrea gigas #1	93.06	56.78	9.26	45.00	21.38	2.10
Crassostrea gigas #2	100.82	59.18	7.22	50.46	23.98	2.10
Crassostrea gigas #3	101.94	43.07	8.84	40.25	19.13	2.10
Crassostrea gigas #4	101.46	53.37	10.62	39.48	18.76	2.10
Crassostrea gigas #5	86.47	60.46	7.71	54.93	26.10	2.10
Crassostrea gigas #6	83.52	53.95	3.39	23.88	11.35	2.10
Crassostrea gigas #7	100.86	51.60	7.05	42.95	20.41	2.10
Crassostrea gigas #8	101.50	57.77	4.54	39.38	18.71	2.10
Average	96.20	54.52	7.33	42.04	19.98	
standard deviation	7.53	5.53	2.40	9.21	4.38	

Oyster XRF map dimensions

#	map width (mm)	map length	#pixels in X-direction	#pixels in Y-direction	Total # of pixels	Spatial resolution (um)
Crassostrea gigas #1	78.10	24.93	3124	997	3114628	25
Crassostrea gigas #2	101.01	33.30	3367	1110	3737370	30
Crassostrea gigas #3	102.00	39.00	3400	1300	442000	30
Crassostrea gigas #4	106.55	26.55	4262	1062	4526244	25
Crassostrea gigas #5	88.30	29.50	3532	1180	4167760	25
Crassostrea gigas #6	85.68	31.53	3427	1261	4321447	25
Crassostrea gigas #7	103.00	20.10	4120	804	3312480	25
Crassostrea gigas #8	102.66	34.80	3422	1160	3969520	30
Average					3946181	26.88
standard deviation					519354	2.59

Model results

#	Shell length (mm)	Shell width (mm)	Average shell thickness (mm)	Shell mass (g)	Shell volume (cm3)	Density
Crassostrea gigas #1	97.31	59.37	4.61	30.66	14.60	2.10
Crassostrea gigas #2	100.45	58.96	4.89	38.65	18.40	2.10
Crassostrea gigas #3	102.34	43.24	5.88	58.26	27.74	2.10
Crassostrea gigas #4	101.08	53.17	6.41	36.57	17.41	2.10
Crassostrea gigas #5	89.56	62.62	4.42	25.66	12.21	2.10
Crassostrea gigas #6	78.80	50.90	3.83	15.85	7.55	2.10
Crassostrea gigas #7	100.74	51.54	4.84	25.78	12.28	2.10
Crassostrea gigas #8	100.59	57.25	5.16	32.97	15.70	2.10
Average	96.36	54.63	5.01	33.05	15.74	
standard deviation	8.17	6.18	0.82	12.47	5.94	

Growth curve fits

#		Shell Length (mm) $L = L_0 * e^{(k*t)}$			Shell thickness (mm) $T = a*t$		Shell mass (g) $M = a*t^e$			Growth rate (g/yr) $dM/dt = a*t$	
Fit parameter	N	L_0	k	R^2	a	R^2	a	e	R^2	a	R^2
Crassostrea gigas #1	700	140.40	0.28	0.95	0.80	0.99	0.20	3.58	0.98	2.53	0.62
Crassostrea gigas #2	900	106.19	0.79	0.91	0.99	0.99	1.53	2.45	0.97	2.86	0.29
Crassostrea gigas #3	600	94.76	11.09	0.25	0.54	0.93	0.87	1.97	0.88	3.45	0.70
Crassostrea gigas #4	700	90.77	44.65	0.17	0.78	0.99	0.78	2.23	0.99	2.13	0.19
Crassostrea gigas #5	700	91.50	2.29	0.98	1.61	0.98	6.58	2.08	0.88	4.77	0.32
Crassostrea gigas #6	600	83.39	1.13	0.98	1.33	0.99	2.66	2.00	0.93	4.06	0.66
Crassostrea gigas #7	800	103.28	1.01	0.91	0.94	0.99	0.66	2.76	0.96	2.44	0.76
Crassostrea gigas #8	482	100.59	4.47	0.76	1.23	0.99	5.99	1.40	0.97	3.59	0.44
Crassostrea gigas composite	4655	102.34	0.99	0.60	0.94	0.91	1.83	1.98	0.76	2.81	0.21

Geoscientific
Model Development
Discussions

Table 3

	species	#	% of map	Mg (µg/g) ± 422	Si (µg/g) ± 148	P (µg/g) ± 4	S (µg/g) ± 121	Ca (µg/g) ± 395	Mn (µg/g) ± 4	Fe (µg/g) ± 6	Zn (µg/g) ± 11	Sr (µg/g) ± 3
Chalky calcite	C.gigas	1	62.53%	-	2384	2	116	383304	27	162	17	297
	C.gigas	2	68.87%	4001	4259	137	5341	374559	98	49	57	1877
	C.gigas	3	59.25%	4393	4934	151	5267	353857	33	7	31	1135
	C.gigas	4	49.55%	2368	4239	44	2891	378539	47	14	23	644
	C.gigas	5	83.91%	1643	3108	73	1627	390939	51	30	57	703
	C.gigas	6	79.12%	1802	2903	81	1923	388243	66	43	27	611
	C.gigas	7	40.40%	1847	4231	70	3097	384371	23	125	20	699
	C.gigas	8	71.97%	4267	5175	182	5921	357400	92	71	52	1358
Foliated calcite	C.gigas	1	37.47%	2744	4732	114	6399	351759	103	261	54	1433
	C.gigas	2	31.13%	1153	3644	78	3920	388370	70	13	75	1432
	C.gigas	3	40.75%	1801	3279	71	3069	381022	30	0	25	1382
	C.gigas	4	50.45%	1304	1455	484	2173	387183	61	39	26	694
	C.gigas	5	16.09%	2112	3837	48	1907	389176	65	138	62	1690
	C.gigas	6	20.88%	1903	6047	81	2040	386690	58	31	22	1510
	C.gigas	7	59.60%	1062	2161	31	1691	392954	38	1	17	728
	C.gigas	8	28.03%	2488	2522	72	4077	380805	78	37	52	1525

Reproducibility error (1σ)